

pubs.acs.org/NanoLett Letter

Strain-Driven Faceting of Graphene-Catalyst Interfaces

Mitisha Surana, Ganesh Ananthakrishnan, Matthew M. Poss, Jad Jean Yaacoub, Kaihao Zhang, Tusher Ahmed, Nikhil Chandra Admal, Pascal Pochet, Harley T. Johnson, and Sameh Tawfick*



Cite This: Nano Lett. 2023, 23, 1659-1665

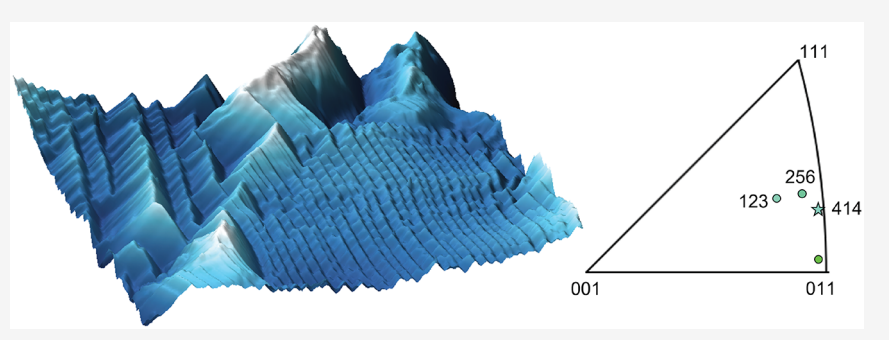


ACCESS I

III Metrics & More

Article Recommendations

s Supporting Information



ABSTRACT: The interfacial interaction of 2D materials with the substrate leads to striking surface faceting affecting its electronic properties. Here, we quantitatively study the orientation-dependent facet topographies observed on the catalyst under graphene using electron backscatter diffraction and atomic force microscopy. The original flat catalyst surface transforms into two facets: a low-energy low-index surface, e.g. (111), and a vicinal (high-index) surface. The critical role of graphene strain, besides anisotropic interfacial energy, in forming the observed topographies is revealed by molecular simulations. These insights are applicable to other 2D/3D heterostructures.

KEYWORDS: graphene, interface mechanics, chemical vapor deposition, surface faceting

The optical and electronic performance of 2D materials synthesized by chemical vapor deposition (CVD) is deeply rooted in its structure, strain state, atomic-scale defects, and interfacial interactions. The emergence of semiconducting graphene, 1,2 surface faceting, 3 and moiré superstructures 1,5 is a manifestation of the strong interfacial interactions. Faceting, in particular, is commonly observed under large single crystals of graphene synthesized on metal catalysts using CVD [Figure 1(a)]. The faceting phenomenon defines the length scale for devices, 6,7 strongly impacting the technological significance of the material.

The faceted structures are ubiquitous—observed on all catalysts, irrespective of their composition or thickness. S-11 They also have a variety of morphologies, showing strong dependence on the surface texture of the substrate. Exhibiting average heights of 40 nm and widths ranging between 100—300 nm, the facets are smooth and planar showing minimal roughness on analysis using Atomic Force Microscopy (AFM). Wang et al. Show that these facets form during cooling of the system in CVD, while Ananthakrishnan et al. Teveal that graphene preserves facets postgrowth. Faceting has also been observed during growth of other materials. The two commonly observed types of faceting in experiments are shown in Figure 1(b). The left figure shows a unidirectional morphology where two inclined planes form a triangular-shaped corrugation. The right figure, referred to as pyramidal,

has one of the two inclined planes being hierarchically faceted, resulting in three planes forming the final surface reconstruction.

The creation of these large, faceted structures is sometimes said to occur by step bunching. This refers to the aggregation of small atomic steps into large steps, while faceting describes the formation of crystalline hill-valley morphology from an arbitrary surface. Step bunching under graphene has been attributed to a variety of factors. Hayashi et al. report a pressure-driven step bunching process due to the evaporation of copper during CVD. A similar kinetic model due to decelerated sublimation of copper atoms is proposed by Wofford et al. Meanwhile, Kang et al. and Deng et al. report the effect of compressive strain due to thermal expansion mismatch between graphene and the substrate driving facet formation. However, Yi and co-workers argue that no strain is released due to step bunching and propose that the fast diffusion of metal atoms under graphene and the

Received: October 6, 2022 Revised: January 31, 2023 Published: February 6, 2023





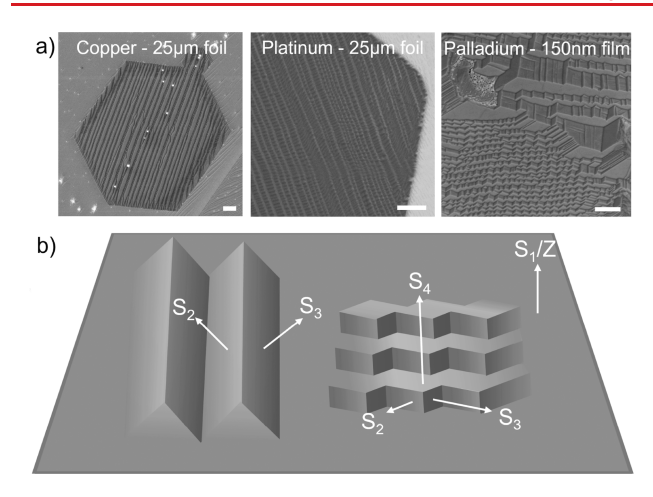


Figure 1. Faceted surfaces and facet terminology. a) Faceted structures imaged using Scanning Electron Microscopy (SEM) observed under graphene flakes after synthesis on different substrates. All scale bars are 1 μ m. b) Schematic representation of facets. S_1/Z represents the crystal orientation of the substrate surface. Left: Unidirectional structure with two facets $-S_2$ and S_3 . Right: Pyramidal structure with three facets $-S_2$, S_3 , and S_4 .

local bending energy of graphene drive step bunching. Despite the importance of this phenomenon, limited quantitative studies analyzing the orientation of the facets have been reported, typically using electron diffraction methods. 17,18

In this work, we use a novel algorithm for fast non-destructive investigation of the crystallographic morphology employing AFM along with Electron Backscatter Diffraction (EBSD). Characterization of the facet orientations enables us to unravel the mechanisms driving faceting of the graphene-covered metal surface. We use the following terminology to define surfaces: S_1 denotes the crystallographic orientation of the flat (basal) plane of the substrate, as shown in Figure 1(b). S_i denotes the i^{th} decomposition of S_1 . For unidirectional faceting, S_1 transforms to S_2 and S_3 [Figure 1(b) - Left]. For pyramidal faceting, S_1 reconstructs into three new facets S_2 , S_3 , and S_4 [Figure 1(b) - Right].

Figure 2 shows the Facet Orientation Analysis (FOA) used to calculate the orientation of the facets using EBSD and AFM.

Owing to the inherent limitations of EBSD, we obtain only Zorientation, S₁, of the crystal grain under graphene [Figure 2(a)]. This is followed by topographical scan of the faceted metal surface using AFM. We extract height profiles from the scan [Figure 2(b)] which are in the reference system of the AFM (RS_{AFM}). Height profiles are taken along the profile axis direction, while the direction of the surface peaks is referred to as the step axis direction. Normals of the facets-planes are calculated using their slopes in RSAFM. These indices are transformed from RS_{AFM} to the sample reference system (RS_{sample}) in EBSD [Figure 2(c)]. The rotation is done using angle (heta) calculated from the SEM image of graphene between the profile axis direction and X_{sample}. We use the orientation mapping matrix 'g' to transform facets from RS_{sample} to the RS_{crystal}, shown in [Figure 2(d)] (See Supporting Information for more details on experimental procedure). Thus, with the above information, we can calculate indices of S_i in the crystal system with eq 1.

$$[g]_{3\times3}[T_{\text{inplane}}]_{3\times3}[S_{i_{\text{AFM}}}]_{3\times1} = [S_{i_{\text{crostal}}}]_{3\times1}$$
 (1

[Figure 2(e)] shows a 2D illustration of unidirectional faceting. To visualize this geometric transformation, we use the Inverse Pole Figures (IPF) [Figure 2(f)], traditionally used in crystal orientation studies. A "star" marker denotes initial orientation S_1 , and "circular" markers represent the S_2 , S_3 surfaces.

Twenty-seven different systems were analyzed using the FOA method to study both unidirectional and pyramidal faceting. Figure 3 reports four such systems and their transformations in the form of IPFs. Invariably, S_1 continuously evolves into a broad range of orientations. One of the facets (S_2) is usually seen to be rotating toward a low-index surfaces (e.g., 111 or 001). But the other facet, S_3 , surprisingly appears to rotate toward a high-energy vicinal orientation. These FOA measurements are corroborated using diffraction patterns of transmission electron microscopy (TEM) [Figure 3(a,b): Right]. The accuracy of the FOA method in determining the facet orientations is $\pm 3^{\circ}$ (see Supporting Information). Figure 3(c) shows an interesting, but commonly observed example of a graphene flake growing on two metal grains of different orientations with unidirectional [Figure 3(c)

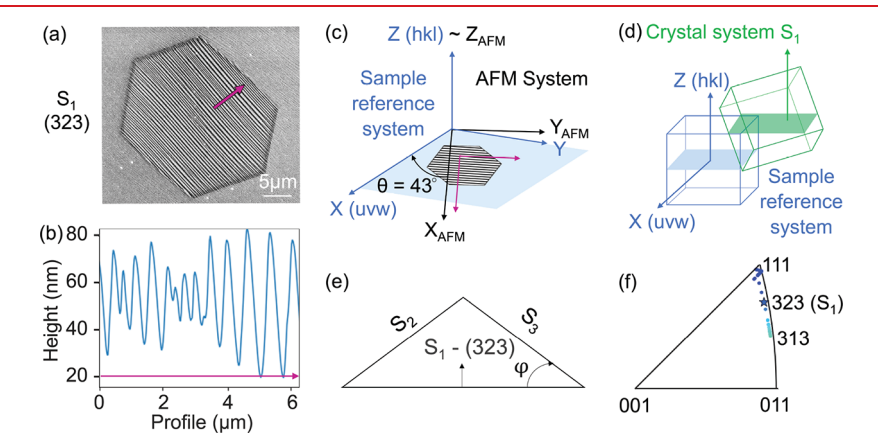


Figure 2. Facet Orientation Analysis (FOA). a) SEM image of a graphene flake on a (323) copper surface obtained from Electron Backscatter Diffraction (EBSD). Magenta arrow - Profile axis direction. b) Height profile from Atomic force microscopy (AFM) along the arrow in (a). c) Schematic of AFM and Sample (EBSD) reference systems. θ - angle between the two reference systems. Dotted magenta arrow - Step axis direction. d) Schematic of Sample and Crystal reference systems. e) Schematic of unidirectional faceting (2D). ϕ - angle between S₁ and S₃. f) Inverse Pole Figure (IPF) showing S₁ (star), S₂, and S₃ for the image in (a), based on FOA.

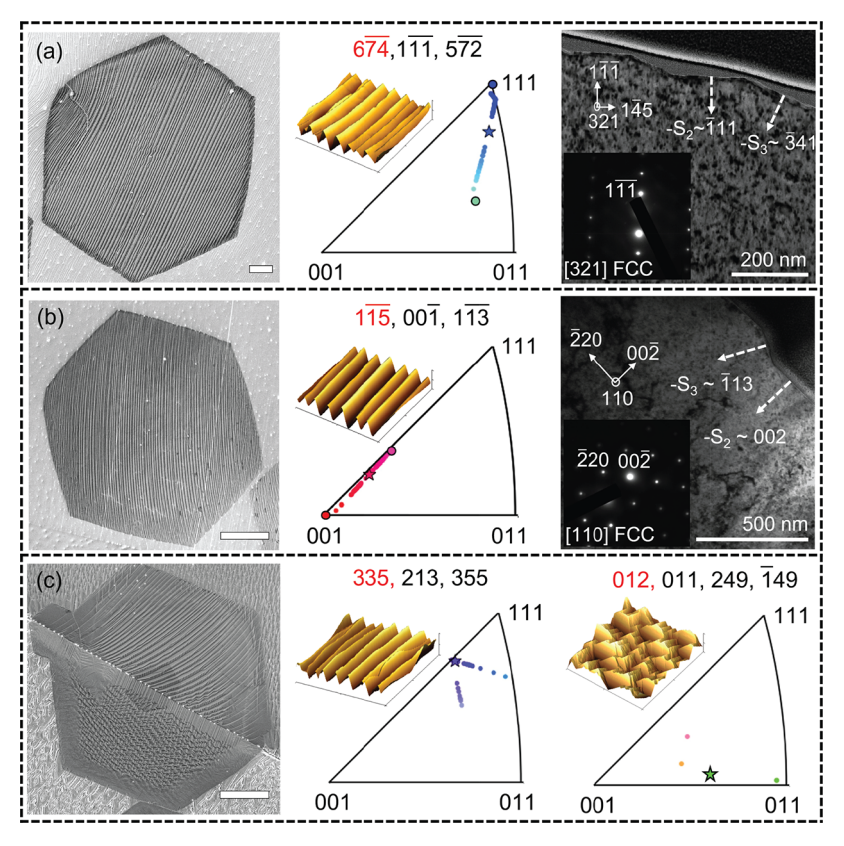


Figure 3. FOA for graphene-copper systems. a, b) From left to right: SEM image of the region analyzed; Miller indices of S_1 (red), approximate S_2 and S_3 (black); 3D AFM scans (inset); IPF plots with S_1 (star), S_2 and S_3 (circles) in standard IPF color scheme. Validation using Transmission electron microscopy (TEM) for respective systems, inset: Diffraction pattern. c) Left: SEM image of graphene on two grains showing unidirectional (above grain boundary) and pyramidal (below grain boundary); Miller indices, AFM scan (inset) and IPF plots of unidirectional (Middle) and pyramidal faceting (Right). Terminology and color convention followed as above. Scale bars for SEM images are 5 μ m.

- Middle] and pyramidal faceting [Figure 3(c) - Right]. The S₂ and S₃ orientations both appear to be going in random directions on the IPF plots in unidirectional case, while in the pyramidal case of Figure 3(c), S_4 appears to be nearly (011), which is a low index surface. Typically, large, consistently oriented facets are observed only under graphene. In some cases, small facets are also observed on the bare copper surface outside the graphene flakes. These facets appear to have consistent size, but unknown orientation uniformity. In some cases, the Cu facets appear to be parallel to those under the graphene as in Figure 3(a). FOA measurements and TEM analysis show that, even when they appear parallel, the facet orientation angles on bare copper surface are different than the graphene-covered surfaces (see Supporting Information Figure S3). We hypothesize that the specific orientation of Cu facets outside graphene is governed by the interplay between impurities and surface energy.

By resolving the crystallographic orientation of the facets, FOA highlights an unexplored energy balance governing these transformations. In a polycrystalline foil produced by rolling processes, the S_1 surface is usually a vicinal orientation with high surface energies. Due to the high temperature growth, the rotation of the S_1 surface to form a low-energy S_2 facet such as (001) or (111) is intuitively favored, indicating the role of surface energy minimization. However, the formation of another vicinal, high-index S_3 orientation as seen in cases (a) and (b) of Figure 3 is intriguing. This has never been reported previously, and in fact contradicts some of the MD simulations in the literature that assume that the facets are low-energy

surfaces.¹¹ Continuum analysis¹⁹ of the effect of surface energy anisotropy and bending rigidity demonstrates faceting qualitatively, but the formation of these vicinal facets is still unclear.

We explore the role of graphene strain on the energy of the graphene-metal system to understand the formation of these high-index orientations calculated using FOA. The mismatch in thermal expansion of graphene and metal substrates during growth causes large interfacial stresses and strains. Moreover, owing to the large size of the graphene domains (>10 μ m), we expect the accumulation of large shear stresses at the interface which can constrict relative slip movements, effectively pinning graphene to the substrate. This effective pinning induces a macroscopic strain in graphene. Hence, in addition to the surface energy minimization driving faceting, we hypothesize that the macroscopic strain, plays a critical, so far hidden, role on the final configuration of faceting.

Molecular statics simulations were performed using LAMMPS²¹ with a hybrid formulation of the interatomic potentials (see Supporting Information). Copper with (323) orientation is used as the substrate in accordance to the experimental observation shown in Figure 2(a). Six facet plane combinations (S_2 - S_3) have been simulated by varying the angle ϕ [Figure 2(e)] between S_3 and S_1 orientation from 60.5° to 0°. Thus, S_3 varies from (111) to (1 0.67 1), the latter being the (323) orientation. S_2 is fixed to (111), mimicking the FOA-calculated low-index orientation. Step height, defined as the number of monatomic steps bunched together to form a large step, ¹¹ is constant and equal to 9 monatomic steps. This

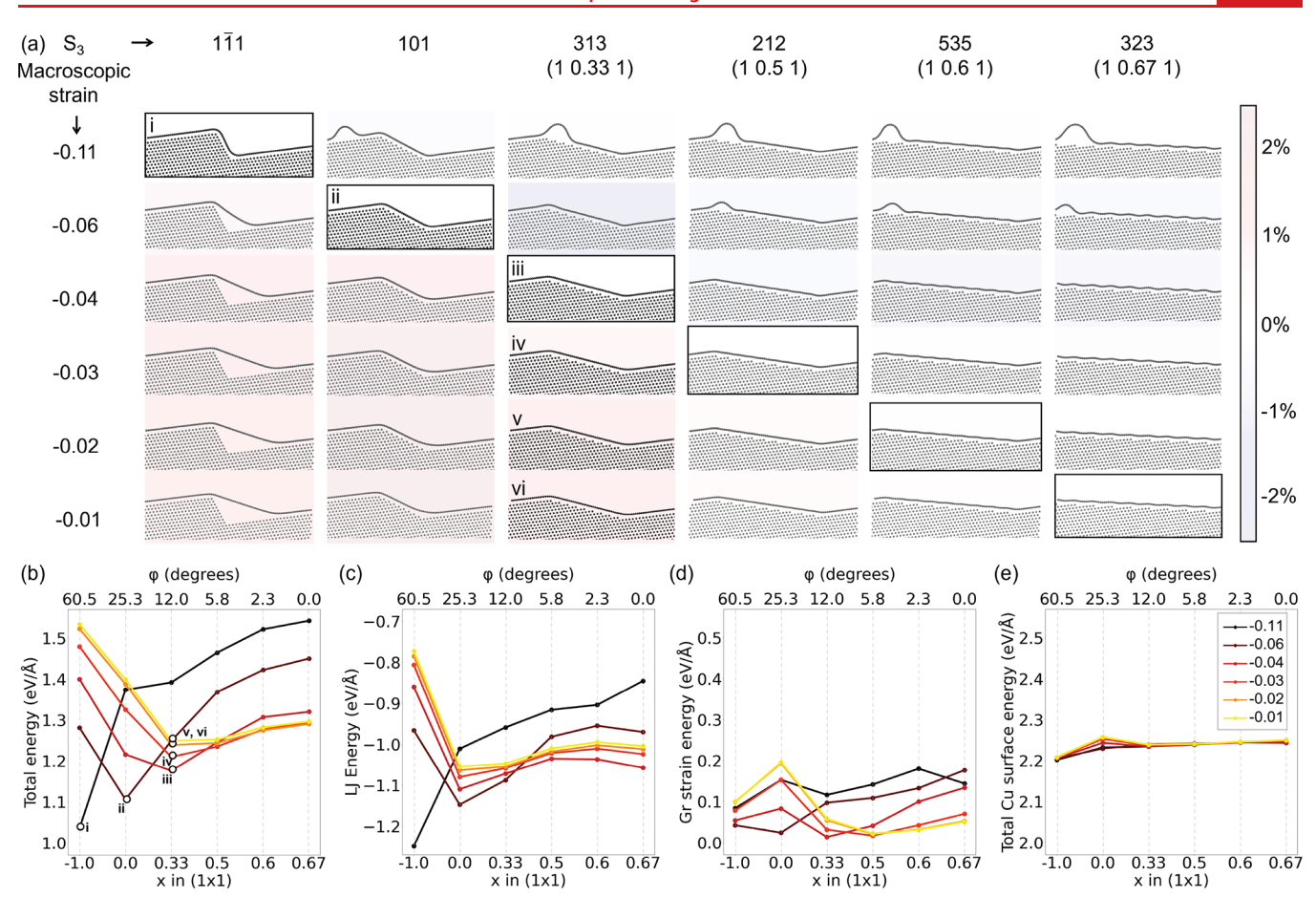


Figure 4. a) Molecular statics simulation of different preliminary macroscopic strains of graphene on copper. $S_1 = (323)$, $S_2 = (111)$, S_3 changes from $(1\overline{1}1)$ to (323) across the columns. The rows indicate the macroscopic strains in the graphene to pin its edges to the cell. The boxed cells show least-strain cases, while the simulation cells (i-vi) represent the S_3 orientation corresponding to the lowest total energy for that specific pinning length. The graphene strains after relaxation are denoted using a colormap: Positive (tensile) in red, and negative (compressive) in blue. b-e) Total energy, Leonard-Jones (LJ) energy between graphene and copper, graphene strain energy and total copper surface energy, per S_1 length, plotted against S_3 orientations for each pinning length, respectively. The lower horizontal axis in plots (b-e) is the x in the (1x1) plane, calculated using the angle ϕ between S_1 and S_3 as indicated on the upper horizontal axis.

allows comparison of trends in energy with respect to S₃ orientation. The columns in Figure 4 are the Miller indices of S₃ in each facet combination. These are represented in further discussions as (1x1). To apply macroscopic strain on graphene, we define pinned length as the total arc-length of graphene which will be compressed and pinned to create the flat S₁ length. Graphene is free to move on the surface of the metal within this length. The pinned length is normalized with the flat S₁ length, and six normalized pinned lengths are selected to induce strains ranging from tensile to compressive after faceting and energy minimization. The macroscopic strain is defined as (1 - normalized pinned length) and is tabulated as rows in Figure 4(a). Pinning is implemented using two rows of graphene atoms that are pinned in the horizontal direction, at the intersection of S_1 (323) surface with each of the S_2-S_3 (111)-(1x1) plane combinations along the step direction [101]. The energy of the system is statically minimized for each combination. The total energy, and its components, divided by the S₁ length, are plotted for each macroscopic strain against the six S_3 orientations in Figure 4(b)-(e). The final strain in graphene is determined for the energy minimized configurations and is represented by the colormap in Figure 4(a). The boxed cells correspond to the facet combination where graphene has least strain, while the cells marked (i)-(vi)

denote the minimum total energy configurations for each induced strain. (See Supporting Information for more details on the simulation setup.)

The lowest energy configuration is found to vary with macroscopic strains. Starting with the longest pinned length, (111) and (111) facet combination exhibits the lowest energy [Figure 4(a)-(i)], which is as expected from a freely sliding graphene (Figure S7 shows the total energy for unpinned graphene on different facet combinations). As the pinned length is reduced, the total energy minima shifts. The shift is seen toward a lower ϕ , or a configuration with a vicinal, higher surface energy S₃ facet - (101) shown in Figure 4(a)-(ii), followed by stabilization at (313) for all smaller pinned lengths [Figure 4 (a)-(iii-vi)]. Importantly, the lowest energy system is not necessarily the configuration with the least strain in graphene. The system is rather reaching a tensile strain, with tension increasing as the pinned length reduces for the same configuration. In general, faceted surfaces with larger ϕ require larger lengths of graphene for better adhesion. For compressive cases seen above the boxed diagonal in Figure 4(a), the strain is released by buckling to form wrinkles in longer pinned lengths. In the tensile cases seen below the boxed diagonal, relaxation occurs by delamination and nonconformality, evident in the (111) - (111) column for small pinned lengths.

The comparable range of LJ interaction energy [Figure 4(c)] and the strain energy [Figure 4(d)] reveals the competition between the two when determining the energy minima of the system, especially looking from (101) to (323) orientation. With increasing tension, graphene can either adhere to the S2 -S₃ facets maximizing the interfacial binding at the cost of taking on strain, or it can delaminate and release tension at the loss of interfacial interaction. The (313) S₃ configuration shows a balance in the amount of strain and LJ interaction, resulting in the minimum total energy configuration observed both in simulation and experimentally. The effect of total Cu surface energy, which includes both strain and surface energy of the faceted copper, is small on the total energy of each configuration [Figure 4 (e)]. Owing to the complex nature of the energy landscape, we perform dynamic simulations only for configurations with a normalized pinned length of 1.04. These simulations involve annealing the systems at 1350 K and subsequent cooling to 0 K. Videos S1, S2, and S3 show the transformation from initial facets of (212), (525) (111) respectively to (111) and approximately (313) under graphene, as expected. The (111)-(313) configuration remains stable as shown in Video S4 (Figure S8 shows the snapshots and Miller indices of final orientations). MD simulations are limited by time to show the transformation of (323) surface to large (111)-(313) facets. Regardless, these simulations confirm that graphene strain mediates faceting. Experimentally, Raman spectroscopy shows the presence of compressive (also reported in literature ^{9,10}) and tensile strains in graphene postgrowth at room temperature [(Figure S4 shows strain present in graphene on copper shown in Figure 2(a)].

We propose a mechanism where final strain in graphene results from both surface energy anisotropy and thermal expansion mismatch. Figure 5 schematically illustrates the

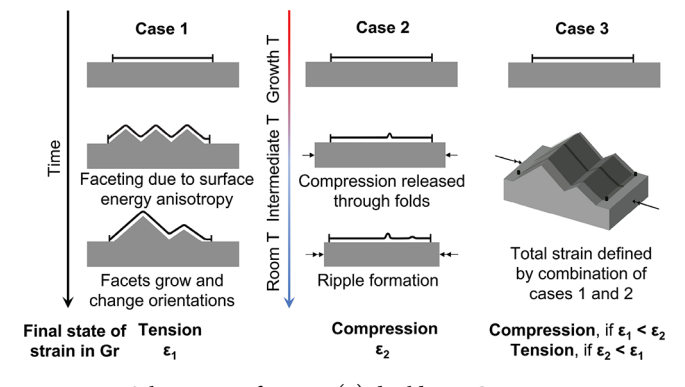


Figure 5. Schematics of strain (ε) build-up. Case 1: Increase in surface area due to faceting at growth temperature induces tension. Case 2: Postgrowth cooling induces compression due to thermal mismatch. Case 3: Strain state of graphene (tension/compression) is due to the combination of cases 1 and 2.

faceting observed in graphene during CVD on metal substrates. Starting with graphene pinned at growth temperature, we consider three cases of graphene-metal interaction. Case 1 explores the pure effect of the geometry of faceting on strain, without the effect of thermal mismatch. Given enough energy and time, facets form by surface specific diffusion in metal as the system lowers its energy. Since graphene is pinned, macroscopic strains are induced. Depending on the availability of thermal energy, these facets may coalesce to release some bending strain, consistent with previous step

bunching studies. Regardless, graphene will have some amount of tensile strain at room temperature (RT). In Case 2, the strain in graphene is considered only due to thermal expansion coefficient mismatch. Graphene has a negative expansion coefficient, while copper contracts during cooling. Owing to this mismatch and graphene being pinned, an overall compressive strain develops in graphene. According to Wang et al., ²² graphene releases most of this strain by the formation of folds at an intermediate temperature of ~750 °C or ripples at lower temperatures. However, at RT, graphene will either be in low compressive stress, or nearly stress-free, if all the strain is released due to rippling.

In a more realistic situation (Case 3), the two competing effects occur simultaneously. Pinned graphene on cooling releases compressive strain due to the thermal mismatch by the formation of both facets and folds, with folds usually forming in a direction perpendicular to the facets. Faceting reduces at lower temperatures due to lesser diffusion, but compressive strain due to thermal mismatch continues to develop which can be released through wrinkling in both directions. Finally, at room temperature, if the total tensile strain due to facets is greater than the final compressive strain, then graphene will be in tension at RT. If the converse is true, graphene will be under compressive stress. Thus, we establish that the presence of strain in graphene at room temperature is a result of the interplay between thermal mismatch and faceting-induced area increase during cooling.

To conclude, the intriguing faceting phenomena observed during graphene growth are studied by a new FOA method combining EBSD, SEM, and AFM, and validated with TEM. Molecular simulations reveal the delicate balance between the anisotropic interfacial surface energy minimization and the graphene strain. Starting with a vicinal surface, the system transforms into facets with at least one low-index low-energy surface. The strain induced in the pinned graphene, developed as a result of surface faceting and thermal mismatch, is responsible for the other facets having an unexpected vicinal orientation. A typical polycrystalline foil has many grains having vicinal surfaces. Graphene growth on each grain is affected by the above-mentioned factors, resulting in the varying morphology observed across the different grains. Regardless, this anomalous faceting improves the interfacial interaction at the cost of graphene strain. We have not examined the effect of kinetics, number of layers, or the size of the facets in our analysis. These topics are worthy of further studies owing to their applicability to charge mobility in devices, 6 catalysis, 23 and remote epitaxy. 24

ASSOCIATED CONTENT

Solution Supporting Information

The Supporting Information is available free of charge at https://pubs.acs.org/doi/10.1021/acs.nanolett.2c03911.

More details on experimental and computational procedures Table S1. CVD growth recipes for different substrates used in the study. Figure S1. 3D scan of the facets taken using AFM, showing line scan and planar analysis. Figure S2. Comparison between planar and line analysis for two example systems. Figure S3. Facet orientations in the presence and absence of graphene using TEM analysis. Figure S4. Raman scans showing negligible amplitude of D peak of graphene grown on copper. Figure S5. Raman scans showing compressive

and tensile strain present in graphene grown on copper. Figure S6. Simulation cell and schematic showing S_1 , S_2 , and S_3 Figure S7. The six faceted combinations, their simulation cells, normalized graphene pinned length, and macroscopic strains present in the system owing to pinning. Figure S8. Molecular dynamic (MD) simulations performed for different initial and final facet configurations with normalized pinned length = 1.04. Figure S9. Effect of step height on the energy of freely sliding graphene on copper for three different orientations (PDF)

Video S1. Dynamic simulation at 1350 K showing the transformation of a large step under graphene with macroscopic strain of -0.04 with S_3 orientation (212) to expected S_3 orientation (313) (MP4)

Video S2. Dynamic simulation at 1350 K showing the transformation of a large step under graphene with macroscopic strain of -0.04 with S_3 orientation (525) to expected S_3 orientation (313) (MP4)

Video S3. Dynamic simulation at 1350 K showing the transformation of a large step under graphene with macroscopic strain of -0.04 with S_3 orientation $(1\ \overline{(1)}1)$ to expected S_3 orientation (313) (MP4)

Video S4. Dynamic simulation at 1350 K showing the stability of a (111)-(313) facet orientation under graphene with macroscopic strain of -0.04 (MP4)

AUTHOR INFORMATION

Corresponding Author

Sameh Tawfick — Department of Mechanical Science and Engineering and The Beckman Institute for Advanced Science and Technology, University of Illinois at Urbana—Champaign, Urbana 61801 Illinois, USA; orcid.org/0000-0003-3645-527X; Email: tawfick@illinois.edu

Authors

Mitisha Surana – Department of Materials Science and Engineering, University of Illinois at Urbana–Champaign, Urbana 61801 Illinois, USA; orcid.org/0000-0002-6316-0197

Ganesh Ananthakrishnan — Department of Materials Science and Engineering, University of Illinois at Urbana—Champaign, Urbana 61801 Illinois, USA; orcid.org/0000-0003-3509-2059

Matthew M. Poss – Department of Mechanical Science and Engineering, University of Illinois at Urbana–Champaign, Urbana 61801 Illinois, USA

Jad Jean Yaacoub – Department of Mechanical Science and Engineering, University of Illinois at Urbana–Champaign, Urbana 61801 Illinois, USA

Kaihao Zhang — The Hong Kong University of Science and Technology, Guangzhou 999077 Hong Kong, China; orcid.org/0000-0003-4804-3715

Tusher Ahmed – Department of Mechanical Science and Engineering, University of Illinois at Urbana–Champaign, Urbana 61801 Illinois, USA

Nikhil Chandra Admal – Department of Mechanical Science and Engineering, University of Illinois at Urbana–Champaign, Urbana 61801 Illinois, USA

Pascal Pochet – Department of Physics, IriG, Univ. Grenoble-Alpes and CEA, Grenoble F-38054, France; ⊚ orcid.org/ 0000-0002-1521-973X Harley T. Johnson – Department of Materials Science and Engineering, University of Illinois at Urbana–Champaign, Urbana 61801 Illinois, USA; Department of Mechanical Science and Engineering, University of Illinois at Urbana–Champaign, Urbana 61801 Illinois, USA

Complete contact information is available at: https://pubs.acs.org/10.1021/acs.nanolett.2c03911

Notes

The authors declare no competing financial interest.

ACKNOWLEDGMENTS

We gratefully acknowledge support from the NSF grant CMMI 18-25300 and the Office of Naval Research ONR N00014-18-1-2457. The SEM, AFM, and TEM analyses were carried out in part in the Materials Research Laboratory Central Research Facilities, University of Illinois. P.P. acknowledges partial support from The French National Research Agency (2D-TRANSFORMERS ANR-14-OHRI-0004).

REFERENCES

- (1) Kwon, S.-Y.; Ciobanu, C. V.; Petrova, V.; Shenoy, V. B.; Bareno, J.; Gambin, V.; Petrov, I.; Kodambaka, S. Growth of semiconducting graphene on palladium. *Nano Lett.* **2009**, *9*, 3985–3990.
- (2) Zhou, S. Y.; Gweon, G.-H.; Fedorov, A. V.; First, P. N.; de Heer, W. A.; Lee, D.-H.; Guinea, F.; Castro Neto, A. H.; Lanzara, A. Substrate-induced bandgap opening in epitaxial graphene. *Nature materials* **2007**, *6*, 770–775.
- (3) Li, X.; Cai, W.; An, J.; Kim, S.; Nah, J.; Yang, D.; Piner, R.; Velamakanni, A.; Jung, I.; Tutuc, E.; et al. Large-area synthesis of high-quality and uniform graphene films on copper foils. *science* **2009**, 324, 1312–1314.
- (4) N'Diaye, A. T.; Bleikamp, S.; Feibelman, P. J.; Michely, T. Two-Dimensional Ir Cluster Lattice on a Graphene Moiré on Ir(111). *Phys. Rev. Lett.* **2006**, *97*, 215501.
- (5) Wintterlin, J.; Bocquet, M.-L. Graphene on metal surfaces. *Surf. Sci.* **2009**, *603*, 1841–1852.
- (6) Ni, G.-X.; Zheng, Y.; Bae, S.; Kim, H. R.; Pachoud, A.; Kim, Y. S.; Tan, C.-L.; Im, D.; Ahn, J.-H.; Hong, B. H.; et al. Quasi-periodic nanoripples in graphene grown by chemical vapor deposition and its impact on charge transport. *ACS Nano* **2012**, *6*, 1158–1164.
- (7) Kim, D. W.; Lee, J.; Kim, S. J.; Jeon, S.; Jung, H.-T. The effects of the crystalline orientation of Cu domains on the formation of nanoripple arrays in CVD-grown graphene on Cu. *Journal of Materials Chemistry C* **2013**, *1*, 7819–7824.
- (8) Hayashi, K.; Sato, S.; Yokoyama, N. Anisotropic graphene growth accompanied by step bunching on a dynamic copper surface. *Nanotechnology* **2013**, *24*, 025603.
- (9) Kang, J. H.; Moon, J.; Kim, D. J.; Kim, Y.; Jo, I.; Jeon, C.; Lee, J.; Hong, B. H. Strain relaxation of graphene layers by Cu surface roughening. *Nano Lett.* **2016**, *16*, 5993–5998.
- (10) Deng, B.; Wu, J.; Zhang, S.; Qi, Y.; Zheng, L.; Yang, H.; Tang, J.; Tong, L.; Zhang, J.; Liu, Z.; et al. Anisotropic strain relaxation of graphene by corrugation on copper crystal surfaces. *Small* **2018**, *14*, 1800725.
- (11) Yi, D.; Luo, D.; Wang, Z.-J.; Dong, J.; Zhang, X.; Willinger, M.-G.; Ruoff, R. S.; Ding, F. What drives metal-surface step bunching in graphene chemical vapor deposition? *Physical review letters* **2018**, *120*, 246101.
- (12) Wang, Z.-J.; Weinberg, G.; Zhang, Q.; Lunkenbein, T.; Klein-Hoffmann, A.; Kurnatowska, M.; Plodinec, M.; Li, Q.; Chi, L.; Schlögl, R.; et al. Direct observation of graphene growth and associated copper substrate dynamics by in situ scanning electron microscopy. ACS Nano 2015, 9, 1506–1519.
- (13) Ananthakrishnan, G.; Surana, M.; Poss, M.; Yaacoub, J. J.; Zhang, K.; Admal, N.; Pochet, P.; Tawfick, S.; Johnson, H. T.

Graphene-mediated stabilization of surface facets on metal substrates. *J. Appl. Phys.* **2021**, *130*, 165302.

- (14) Lin, J.; Tay, R. Y.; Li, H.; Jing, L.; Tsang, S. H.; Wang, H.; Zhu, M.; McCulloch, D. G.; Teo, E. H. T. Smoothening of wrinkles in CVD-grown hexagonal boron nitride films. *Nanoscale* **2018**, *10*, 16243–16251.
- (15) Wang, L.; Xu, X.; Zhang, L.; Qiao, R.; Wu, M.; Wang, Z.; Zhang, S.; Liang, J.; Zhang, Z.; Zhang, Z.; et al. Epitaxial growth of a 100-square-centimetre single-crystal hexagonal boron nitride monolayer on copper. *Nature* **2019**, *570*, 91–95.
- (16) Wofford, J. M.; Nie, S.; McCarty, K. F.; Bartelt, N. C.; Dubon, O. D. Graphene islands on Cu foils: the interplay between shape, orientation, and defects. *Nano Lett.* **2010**, *10*, 4890–4896.
- (17) Vondráček, M.; Kalita, D.; Kučera, M.; Fekete, L.; Kopeček, J.; Lančok, J.; Coraux, J.; Bouchiat, V.; Honolka, J. Nanofaceting as a stamp for periodic graphene charge carrier modulations. *Sci. Rep.* **2016**, *6*, 1–7.
- (18) Schädlich, P.; Speck, F.; Bouhafs, C.; Mishra, N.; Forti, S.; Coletti, C.; Seyller, T. Stacking Relations and Substrate Interaction of Graphene on Copper Foil. *Advanced Materials Interfaces* **2021**, *8*, 2002025.
- (19) Surana, M.; Ahmed, T.; Admal, N. C. Interface mechanics of 2D materials on metal substrates. *Journal of the Mechanics and Physics of Solids* **2022**, *163*, 104831.
- (20) Bronsgeest, M. S.; Bendiab, N.; Mathur, S.; Kimouche, A.; Johnson, H. T.; Coraux, J.; Pochet, P. Strain relaxation in CVD graphene: wrinkling with shear lag. *Nano Lett.* **2015**, *15*, 5098–5104.
- (21) Thompson, A. P.; Aktulga, H. M.; Berger, R.; Bolintineanu, D. S.; Brown, W. M.; Crozier, P. S.; in't Veld, P. J.; Kohlmeyer, A.; Moore, S. G.; Nguyen, T. D.; et al. LAMMPS-a flexible simulation tool for particle-based materials modeling at the atomic, meso, and continuum scales. *Comput. Phys. Commun.* 2022, 271, 108171.
- (22) Wang, M.; Huang, M.; Luo, D.; Li, Y.; Choe, M.; Seong, W. K.; Kim, M.; Jin, S.; Wang, M.; Chatterjee, S.; et al. Single-crystal, large-area, fold-free monolayer graphene. *Nature* **2021**, *596*, 519–524.
- (23) Kim, J. Y.; Park, W.; Choi, C.; Kim, G.; Cho, K. M.; Lim, J.; Kim, S. J.; Al-Saggaf, A.; Gereige, I.; Lee, H.; Jung, W.-B.; Jung, Y.; Jung, H.-T. High Facets on Nanowrinkled Cu via Chemical Vapor Deposition Graphene Growth for Efficient CO2 Reduction into Ethanol. ACS Catal. 2021, 11, 5658–5665.
- (24) Kim, Y.; Cruz, S. S.; Lee, K.; Alawode, B. O.; Choi, C.; Song, Y.; Johnson, J. M.; Heidelberger, C.; Kong, W.; Choi, S.; et al. Remote epitaxy through graphene enables two-dimensional material-based layer transfer. *Nature* **2017**, *544*, 340–343.

□ Recommended by ACS

Real-Space Mapping of Local Subdegree Lattice Rotations in Low-Angle Twisted Bilayer Graphene

Ya-Ning Ren, Lin He, et al.

FEBRUARY 17, 2023

NANO LETTERS

READ 🗹

Modulation of Remote Epitaxial Heterointerface by Graphene-Assisted Attenuative Charge Transfer

Yuning Wang, Ke Xu, et al.

FEBRUARY 06, 2023

ACS NANO

READ 🗹

Artificial Graphene Nanoribbons: A Test Bed for Topology and Low-Dimensional Dirac Physics

Daniel J. Trainer, Nathan P. Guisinger, et al.

AUGUST 15, 2022

ACS NANO

READ

Graphene Capping of Cu Back-End-of-Line Interconnects Reduces Resistance and Improves Electromigration Lifetime

Keun Wook Shin, Kyung-Eun Byun, et al.

MARCH 14, 2023

ACS APPLIED NANO MATERIALS

READ 🗹

Get More Suggestions >